Reduced and Reformulated Electrochemical Model-based Detection and Isolation of Electrode-level Faults in Lithium-ion Battery Cells *

Shanthan Kumar Padisala. Sara Sattarzadeh. Satadru Dey.

The Pennsylvania State University, University Park, PA 16802 USA (e-mail: sfp5587@psu.edu, sfs6216@psu.edu, skd5685@psu.edu).

Abstract: Despite finding their usage in multiple applications ranging from mobile phones to electric vehicles, degradation of Lithium-ion batteries and fault occurrences over a period of time, is still inevitable. There are numerous types of degradation and faults that are possible in a battery. Some of these faults affect individual electrodes (cathode and anode) of the battery while some of them manifest themselves on the battery cell as a whole. Diagnostics of cell-level faults has been explored extensively while electrode-level fault detection has received relatively lesser attention. In this work, we attempt to detect and isolate certain type of faults occurred in battery electrodes and distinguish if the fault has primarily occurred in the anode or the cathode. We utilize a reduced order and reformulated electrochemical models along with feedback-based observers to realize the proposed method. Preliminary simulation-based case studies are shown to illustrate the proposed approach.

Keywords: Li-ion Batteries, Fault Diagnosis, Electrode-level fault detection and isolation.

1. INTRODUCTION

Addressing battery safety is essential for the wide acceptance of Lithium-ion battery technology. Real-time fault diagnostics can help achieve better safety in batteries. In this context, we propose a detection and isolation algorithm for electrode-level faults in Lithium-ion batteries. In existing literature, some works have explored cell-level fault detection based on various types of models Dey and Ayalew (2015); Liu et al. (2014). However, such approaches typically do not provide information on individual electrode-level faults.

Generally speaking, electrode-level estimation has received lesser attention than cell-level estimation. The lack of full observability of electrode states from terminal voltage feedback is a major hindrance to electrode-level estimation algorithms. Some works have attempted to overcome such limitations. For example, observer and filter based approaches are presented in Dey and Ayalew (2017), Moura et al. (2016), Allam and Onori (2018), Allam and Onori (2020), Alavi et al. (2013), and Zhang et al. (2021), and a neural network based approach was presented in Li et al. (2021). However, most of these works assume model parameters are known or ignore the effect of model inaccuracies arising from fault occurrences or do not consider the observability issue. In Dey et al. (2020) an approach to simultaneously estimate the electrode-level charge and health based on a simplified phenomenological type battery model is presented. Sattarzadeh et al. (2020) extended this approach by accounting for electrode-level dynamics, solid electrolyte interface (SEI) growth and nonlinear electrode resistances. Although these works consider parametric variations and estimate them in real-time - they utilize phenomenological models which have limited capability to capture internal physics. Furthermore, most of these observers are designed under non-faulty conditions. Given the fact that a model might change significantly under occurrences of faults - the efficacy of these observers may not be guaranteed under faulty conditions. Electrode-level capacity and utilization window have been estimated in Mohtat et al. (2019). However, the capacity information may not always quickly capture the electrode-level fault signatures. In Lee and Kim (2020), a machine learning based approach was presented for electrode health diagnosis. However, requirement of meaningful and sufficient data is essential for such data-driven techniques which may not always be available.

In this work, we attempt to address some of these research gaps and propose a novel idea using an observer-based framework for electrode-level fault detection and isolation. This work follows the cascaded observer framework devised in Dey et al. (2020) and Sattarzadeh et al. (2020) - with the following differences: (i) Dey et al. (2020) and Sattarzadeh et al. (2020) utilized phenomenoligical battery models that do not consider Lithium concentration distribution within the electrodes while the current work utilizes reduced electrochemical model that considers Lithium concentration distribution within the electrodes; (ii) the observers in Dey et al. (2020) and Sattarzadeh et al. (2020) were designed for state and parameter estimation while

^{*} This work was supported by National Science Foundation under Grant No. 2050315. The opinions, findings, and conclusions or recommendations expressed are those of the author(s) and do not necessarily reflect the views of the National Science Foundation.

the observers in the current work are designed to generate residuals for fault detection and isolation. Specifically, a combination of closed-loop and open-loop observers are chosen in the current work where the difference between the state estimates are used as residual signals which determine the existence of a battery fault. Furthermore, the observer gains follow a rule-based adaptation strategy where different gains are employed to enable initial error convergence and detection of faults, respectively.

The rest of the paper is organized as follows. Section 2 describes the model being considered for the battery and discusses the problem formulation. Fault detection and isolation algorithm is presented in detail in section 3. The applicability of the algorithm is validated by various case studies in section 4 through simulations. Finally, section 5 concludes the paper.

2. MODELING AND PROBLEM STATEMENT

2.1 Single particle electrochemical model

In this work, we have adopted the Single Particle Model (SPM) to capture battery cell electrochemical behavior as described in Rahn and Wang (2013). In SPM, electrodes are modeled as spherical particles with volume-averaging assumption. This results in two linear PDEs that describe the diffusion of lithium ions in the two spherical electrode particles. The resulting PDEs and their corresponding boundary conditions are as follows:

$$\frac{\partial S^{\pm}}{\partial t} = \frac{D_s^{\pm}}{r^2} \frac{\partial}{\partial r} \left(r^2 \frac{\partial S^{\pm}}{\partial r} \right),\tag{1}$$

$$\frac{\partial S^{\pm}}{\partial t} = \frac{D_s^{\pm}}{r^2} \frac{\partial}{\partial r} \left(r^2 \frac{\partial S^{\pm}}{\partial r} \right), \qquad (1)$$

$$\frac{\partial S^{\pm}}{\partial r}|_{r=0} = 0; \frac{\partial S^{\pm}}{\partial r}|_{r=R^{\pm}} = \frac{\pm I}{a_s^{\pm} F D_s^{\pm} A L^{\pm}} \qquad (2)$$

where the superscript \pm indicates positive and negative electrodes, S is the Lithium concentration $[mol/m^3]$, I is the input current [A], where positive current represents the current from the battery (dis-charging), a_s is the specific surface area $[m^2/m^3]$, F is Faraday's constant, D_s is effective diffusion coefficient in solid phase $[m^2/s]$, R is the radius of the particle [m], A is the area of the current collector $[m^2]$ and L is the length of the electrode [m]. Typically, voltage is computed can be done using different models like - Rahn and Wang (2013) and Marcicki et al. (2013), depending upon the complexities and approximations. In the current work the former reduced-order SPM has been adopted for the voltage output evaluation which ignores the mass and charge dynamics in the electrolyte:

$$V = U^{+}(S_{r=R^{+}}^{+}) + \frac{\overline{R}T}{\alpha^{+}F} \sinh^{-1}\left(\frac{I}{2a_{s}^{+}AL^{+}i_{0}^{+}}\right) - U^{-}(S_{r=R^{-}}^{-}) - \frac{\overline{R}T}{\alpha^{-}F} \sinh^{-1}\left(\frac{I}{2a_{s}^{-}AL^{-}i_{0}^{-}}\right) - IR_{f},$$
(5)

where i_0 is the exchange current density of the electrode $[A/m^2]$, U is the open circuit potential of the electrode [V], \overline{R} is the Universal Gas constant and α is the charge transfer coefficient.

2.2 Electrochemical model approximation

For approximating the electrochemical model in (1)-(3), we follow the steps given below:

Step 1 (Finite difference approximation): The PDE system (1)-(2) is approximated to a finite dimensional ODE system by applying finite difference method. The resulting discretized concentration states in positive and negative electrodes are denoted by $x_p = [S_1^+, \cdots, S_N^+]$ and $x_n = [S_1^-, \cdots, S_N^-]$, respectively. Ultimately, we end up with two coupled subsystems:

$$\dot{x}_n = A_n x_n + B_n u, \quad \dot{x}_p = A_p x_p + B_p u,$$
 (4)

$$y = f_{pe}(x_p, u) - f_{ne}(x_n, u) - uR_f,$$
 (5)

where x_p -subsystem captures the positive electrode, x_n subsystem captures the negative electrode, and u is the current. The functions $f_{pe}(.)$ and $f_{ne}(.)$ capture the first two terms, and third and fourth terms, on the right side of (3), respectively.

Step 2 (Dealing with unobservability): Unobservability of individual electrode states from terminal voltage of the battery cell still poses difficulties in the model (4)-(5). To address this, we adopt the framework developed in Dey et al. (2020); Sattarzadeh et al. (2020). Following this framework, the original system is decoupled into two sub-systems: one that accounts for the cathode's dynamics and the other that accounts for the anode's dynamics. In addition to that, for the cathode subsystem voltage equation, we treat the anode contributions as uncertainties. The resulting cathode subsystem is written as

$$\dot{x}_p = A_p x_p + B_p u, \ y = f_{pe}(x_p, u) - \delta_p - u R_f,$$
 (6) where δ_p is the anode potential contribution treated as uncertainty. Similarly, the anode subsystem is written as

 $\dot{x}_n = A_n x_p + B_n u, \ y = \delta_n - f_{ne}(x_n, u) - u R_f,$ where δ_n is the cathode potential contribution treated as uncertainty. In effect, we reformulated the original unobservable system into two decoupled observable but uncertain subsystems.

Step 3 (Linear approximation): In the reformulated model, we still have nonlinear terms $f_{pe}(.)$ and $f_{ne}(.)$ in the output of (6)-(7). In order to linearize these nonlinearities, we approximate the nonlinear functions as piece-wise linear functions. A piece-wise linear approximation example is shown in Fig. 1. The approximations are written as

$$f_{pe}(x_p) \approx C_{p_i} x_p + k_{p_i} + \mu_{p_i}(u), i = \{1, 2\}$$
 (8)

$$f_{ne}(x_n, u) \approx C_{n_i} x_n + k_{n_i} + \mu_{n_i}(u), i = \{1, 2, 3\}$$
 (9)

where i indicates the operating region where the approximation is applied. Note that the coefficients/functions $\{C_{p_i}, k_{p_i}, \mu_{p_i}\}$ and $\{C_{n_i}, k_{n_i}, \mu_{n_i}\}$ vary based on the operating range of x_p and x_n , respectively. Ultimately, we end up with the following two subsystems:

$$\dot{x}_p = A_p x_p + B_p u, \ y = C_{p_i} x_p + k_{p_i} + \bar{\mu}_{p_i}(u) - \delta_p, \quad (10)$$

$$\dot{x}_n = A_n x_p + B_n u, \ y = \delta_{n_i} - C_{n_i} x_n - k_{n_i} - \bar{\mu}_n, \quad (11)$$

$$x_n = A_n x_p + B_n u, \ y = \delta_{n_i} - C_{n_i} x_n - k_{n_i} - \mu_n,$$
 (11)
where $i = \{1, 2\}$ for (10) and $i = \{1, 2, 3\}$ for (11)

where
$$i = \{1, 2\}$$
 for (10) and $i = \{1, 2, 3\}$ for (11), $\bar{\mu}_{p_i}(u) = \mu_{p_i}(u) - uR_f$, and $\bar{\mu}_{n_i}(u) = \mu_{n_i}(u) - uR_f$.

Step 4 (Introduction of filtered voltage state): Following the framework in Dey et al. (2020) and Sattarzadeh et al. (2020), the output voltage is filtered using the filter relation: $\dot{y}_f = -\frac{1}{\tau}y_f + \frac{1}{\tau}y$ where y_f is the filtered output, y is measured output voltage and τ is the filter parameter. The reason behind adding the filter state is that it moves the uncertainties δ_p and δ_n in (10)-(11) from the output equation to the state dynamics equation. The uncertainties in the state dynamics are easier to deal with in the

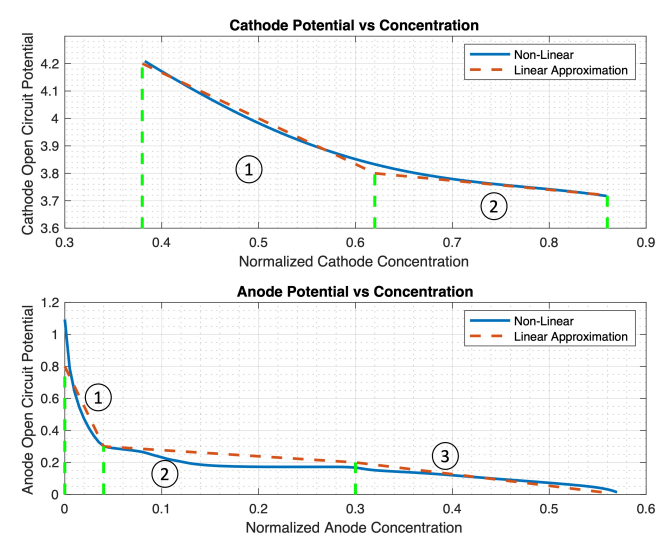


Fig. 1. Piece-wise linearization of electrodes' open circuit potential functions $f_{pe}(.)$ and $f_{ne}(.)$

filter design process, as compared to uncertainties in the output equation. The augmented state-space models after accounting the dynamics of the voltage filter, now become the state-space form listed in (12) and (13).

$$\dot{X}_{p} = \bar{A}_{p_{i}} X_{p} + \bar{B}_{p} U_{p_{i}} + \bar{B}_{p\delta} \delta_{p}, \ Y_{p} = C X_{p},$$
 (12)

$$\dot{X}_n = \bar{A}_{n_i} X_n + \bar{B}_n U_{n_i} + \bar{B}_{n\delta} \delta_n, \ Y_n = C X_n, \tag{13}$$

where

$$\bar{A}_{p_{i}} = \begin{bmatrix} A_{p} & \begin{bmatrix} 0 \\ 0 \\ \vdots \\ 0 \end{bmatrix}, \bar{A}_{n_{i}} = \begin{bmatrix} A_{n} & \begin{bmatrix} 0 \\ 0 \\ \vdots \\ 0 \end{bmatrix}, \\
[0,0,0...,\frac{C_{p_{i}}}{\tau}] & -\frac{1}{\tau} \end{bmatrix}, \bar{A}_{n_{i}} = \begin{bmatrix} A_{n} & \begin{bmatrix} 0 \\ 0 \\ \vdots \\ 0 \end{bmatrix}, \\
[0,0,0...,\frac{C_{n_{i}}}{\tau}] & -\frac{1}{\tau} \end{bmatrix}, \\
\bar{B}_{p} = \bar{B}_{n} = \begin{bmatrix} 0 & 0 & 0 \\ \vdots & \vdots & \vdots \\ -\frac{R_{f}}{\tau} & \frac{1}{\tau} & \frac{1}{\tau} \end{bmatrix}, \bar{B}_{p\delta} = \bar{B}_{n\delta} = \begin{bmatrix} 0 \\ 0 \\ ... \\ -\frac{1}{\tau} \end{bmatrix}, C^{T} = \begin{bmatrix} 0 \\ 0 \\ ... \\ 1 \end{bmatrix}$$

$$X_{p} = \begin{bmatrix} x_{p} \\ y_{p_{f}} \end{bmatrix}, X_{n} = \begin{bmatrix} x_{n} \\ y_{n_{f}} \end{bmatrix}, U_{p_{i}} = \begin{bmatrix} u \\ k_{p_{i}} \\ u_{p_{i}} \end{bmatrix}, U_{n_{i}} = \begin{bmatrix} u \\ k_{n_{i}} \\ u_{p_{i}} \end{bmatrix}.$$

with y_{p_f} and y_{n_f} being the filtered voltage used in cathode and anode models, respectively.

2.3 Problem statement

In the current work, we focus on the detection of internal faults, which are typically difficult to be detected, and then we isolate the faults to the electrode level to distinguish if the fault is from the anode or the cathode.

$$\dot{X}_p = \bar{A}_{p_i} X_p + \bar{B}_p U_{p_i} + \bar{B}_{p\delta} \delta_p + F_p, \ Y_p = C X_p,$$
 (14)

$$\dot{X}_n = \bar{A}_{n_i} X_n + \bar{B}_n U_{n_i} + \bar{B}_{n\delta} \delta_n + F_n, \ Y_n = C X_n, \ (15)$$

In the above two equations, F_p and F_n are the cathode and anode faults, respectively that can arise due to numerous types of battery degradation. Rahimian et al. (2012) describes a very detailed modeling of such faults. Here, the fault behavior is mimicked by changing the model parameters.

3. FAULT DETECTION AND ISOLATION ALGORITHM

A schematic of the framework is illustrated in Fig 2. It consists of two residual generators - Anode and Cathode Residual Generator. Both of them use terminal voltage feedback. In addition, the Anode Residual Generator also receives cathode potential estimate from the Cathode Residual Generator.

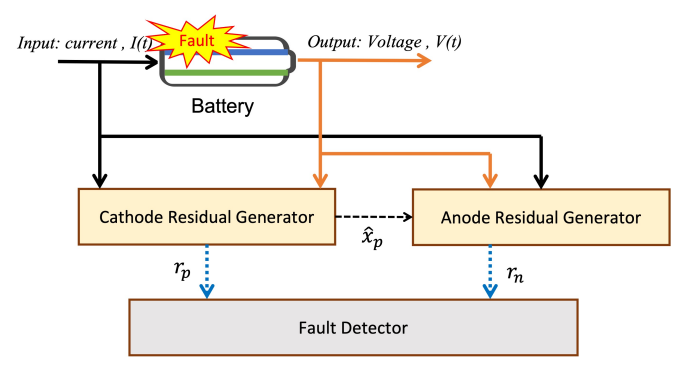


Fig. 2. Schematic of the fault detection and isolation algorithm.

Structure of Cathode Residual Generator: The residual is generated by subtracting the state predictions of the closed-loop observer and the open-loop observer. The open-loop observer is given by a copy of the nominal model (without the uncertainty and the fault):

$$\dot{X}_{p-OL} = \bar{A}_{p_i} X_{p-OL} + \bar{B}_p U_{p_i},$$
 (16)

where X_{p-OL} is the estimated state by the open-loop observer. The closed-loop observer is given by a copy of the nominal model and a feedback term.

 $\dot{X}_{p-CL} = \bar{A}_{p_i} X_{p-CL} + \bar{B}_p U_{p_i} + L_p (Y_p - Y_{p-CL}), \quad (17)$ where X_{p-CL} is the estimated state by the closed-loop observer, Y_p is the measured output, $Y_{p-CL} = C X_{p-CL}$ is the estimated output, and L_p is the observer gain to be designed. Note that the operating region dependent matrix A_{p_i} and input U_{p_i} are calculated using the estimate X_{p-CL} . Ultimately, the Cathode Residual is defined as: $r_p = K(X_{p-CL} - X_{p-OL})$ where $K = [0_{N-1}, 1, 0]$ with 0_{N-1} is a N-1 dimensional row vector of zeros. Effectively, the vector K selects the surface concentration state from the estimated state vector.

Structure of Anode Residual Generator: The residual is generated by subtracting the state predictions of the closed-loop observer and the open-loop observer. The open-loop observer is given by a copy of the nominal model (with an estimated uncertainty and without the fault):

$$\dot{X}_{n-OL} = \bar{A}_{n_i} X_{n-OL} + \bar{B}_n U_{n_i} + \bar{B}_{n\delta} \hat{\delta}_n, \qquad (18)$$

where X_{n-OL} is the estimated state by the open-loop observer. The term $\hat{\delta}_n = f_{pe}(X_{p-CL})$ is the estimate of the uncertainty based on the cathode closed-loop observer estimates. The closed-loop observer is given by:

$$\dot{X}_{n-CL} = \bar{A}_{n_i} X_{n-CL} + \bar{B}_n U_{n_i}
+ \bar{B}_{n\delta} \hat{\delta}_n + L_n (Y_n - Y_{n-CL}),$$
(19)

where X_{n-CL} is the estimated state by the closed-loop observer, Y_n is the measured output, $Y_{n-CL} = CX_{n-CL}$ is the estimated output, and L_n is the observer gain to

be designed. Note that the operating region dependent matrix A_{n_i} and input U_{n_i} are calculated using the estimate X_{n-CL} . Ultimately, the Anode Residual is defined as: $r_n = K(X_{n-CL} - X_{n-OL})$.

3.1 Working principle of the residual generators

In the beginning of the cell operation, only the closed-loop observers were deployed with incorrect initial conditions. Due to the use of output error feedback, the closed-loop observer starts converging. Note that due to the presence of uncertainty terms δ_p and δ_n the steady-state is within an acceptable non-zero bound. This convergence process is fast enough due to the choice of observer gains (e.g. within the first cycle) and we assume that during this process faults do not occur. Based on offline simulations, we can estimate an upper bound of this convergence time t_{conv} for the closed-loop observers. Once t_{conv} is reached, we deploy the open-loop observers and initialize them with the estimate from closed-loop observers, and we also start computing the residuals r_p and r_n . Note that at the moment we turn on the open-loop observer, the difference between open-loop and closed-loop estimates are zero since we are initializing the open-loop observer with closed-loop estimates. Accordingly, we have $r_p = r_n = 0$ at $t = t_{conv}$. However, since there is no output feedback, the openloop observers' performance degrades slightly due to the presence of uncertainty terms δ_p and δ_n . At the same time, the closed-loop observers keep estimating the true states with reasonable accuracy. Accordingly, due to the differences between open and closed-loop observers, the residuals reach a non-zero steady-state after some time.

In the presence of faults, the closed-loop observers are still able to suppress the effect of the fault to a certain extent due to the presence of output error feedback. However, since there is no output feedback in the open-loop observer, the open-loop estimates starts deviating further from the true values. In effect, the residuals start diverging from its previous converged steady-state values. When such divergence is large enough, the fault is detected.

Case-1 Anode Fault: The cathode states are non-faulty which means both the cathode closed-loop and open-loop estimates are close to the true states. This means the cathode residual will not be affected by anode faults. However, the anode open-loop estimates are incorrect while the anode closed-loop estimates are close to the true states. This means that anode residual will be affected and will start diverging. In summary, only anode residual will show the effect under anode faults.

Case-2 Cathode Fault: The cathode open-loop estimates are incorrect while the cathode closed-loop estimates are close to the true states. This means that cathode residual will be affected and will start diverging. On the other hand, the anode open-loop and closed-loop estimates utilize $\hat{\delta}_n = f_{pe}(X_{p-CL})$ as shown in (19) and (18). Hence, the effect of cathode fault might also show up significantly in anode residual. In summary, both anode and cathode residuals can potentially show the effect under cathode faults.

During the process of closed-loop observer design and testing, we have found that one set of observer gains do not

provide optimal performance for initial error convergence and detection of faults. Hence, two sets of gains are used. The first set of gains are used initially until t_{conv} is reached, and then the observer gains are updated to the second set of gains suitable for fault detection. Such gain adaptation will provide better performance as compared to just using one set of gains.

Observer Gain Design: As mentioned before, we design two sets of observer gains. (Gain Set # 1) for convergence against initial condition error. (Gain Set # 2) for fault detection and isolation. For (Gain Set # 1), we check the following: (a) For anode closed-loop observer the gain L_n should be chosen such that the matrix $(\bar{A}_{n_i} L_nC$) is Hurwitz stable $\forall i = \{1, 2, 3\}$, and the estimation error convergence rate is within acceptable limit. (b) For cathode closed-loop observer the gain L_p should be chosen such that the matrix $(\bar{A}_{p_i} - L_p C)$ is Hurwitz stable $\forall i = \{1, 2\},$ and the estimation error convergence rate is within acceptable limit. For (Gain Set # 2), we check the following: (a) For anode closed-loop observer the gain L_n should be chosen such that the matrix $(A_{n_i} - L_n C)$ is Hurwitz stable $\forall i = \{1, 2, 3\}$, and the residual r_n is sensitive to the fault occurrences. (b) For cathode closedloop observer the gain L_p should be chosen such that the matrix $(\bar{A}_{p_i} - L_p C)$ is Hurwitz stable $\forall i = \{1, 2\}$, and the residual r_p is sensitive to the fault occurrences. Qualitatively speaking, (Gain Set # 1) consist of higher values while (Gain Set # 2) consists of lower values. This is because we needed more feedback amplification to counter the initial condition error while lesser feedback amplification is needed for residual sensitivity.

Algorithm 1 Detection algorithm workflow.

(1) Initialization:

- (a) Initialize closed-loop observers of each electrode with incorrect initial conditions.
- (b) Use (Gain Set # 1) for initial error convergence.

(2) Initial run:

Run the closed-loop observers until $t = t_{conv}$.

(3) Update observers:

- (a) Deploy open-loop observers with initial conditions as the state estimates from closed-loop observers at $t=t_{conv}$.
- (b) Update the closed-loop observer gains to (Gain Set # 2).

(4) Detection and isolation of the faults:

(a) Faults are detected and isolated using the criteria listed in Table 1.

Table 1. Fault detection logic

Residual (r_p)	Residual (r_n)	Fault Detection
High	High/Low	Cathode Fault
Low	High	Anode Fault
Low	Low	No Fault

Threshold selection: In reality such modeling uncertainties, disturbances, and measurement noises exist which prohibits the system's natural behavior of zero steady-state residual even in the absence of a fault. To deal with this issue, we followed an approach in Dey et al. (2017) to set threshold limits determined from the non-faulty cases. A residual is HIGH if $\underline{\theta}_{p/n} < r_{p/n} < \overline{\theta}_{p/n}$; a residual is

LOW when $\underline{\theta}_{p/n} > r_{p/n}$ and/or $r_{p/n} > \overline{\theta}_{p/n}$. Here, $\overline{\theta}$ and θ are the upper and lower limits, respectively.

4. CASE STUDIES

The reduced order electrochemical battery model and its corresponding observers for each electrode are constructed and simulated in MATLAB/Simulink. It is observed that the cathode closed-loop observer gives an error of around 0.54% while the anode closed-loop observer shows an error less than 5%. Next, we show some case studies to illustrate the proposed approach. The case studies are performed under a dynamic current profile derived from Urban Dynamometer Driving Schedule (UDDS) cycle. Figure 3 shows the convergence of the closed-loop observer estimates to the original values, starting from incorrect initial conditions. As seen from the from Fig. 3, the convergence time t_{conv} is 2000 s. Accordingly to Algorithm 1, this is the time when we update the closed-loop observer gains and start deploying the open-loop observer. Next, we illustrate three different possibilities: no fault case, anode fault case, and cathode fault case.

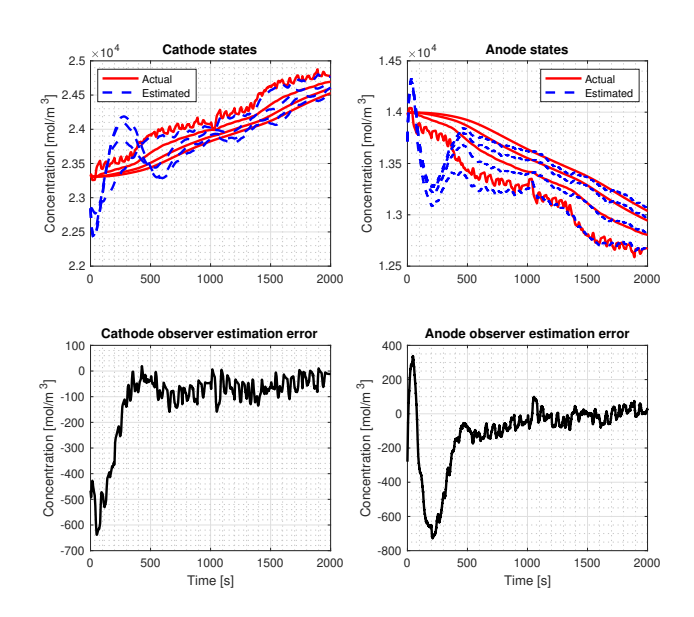


Fig. 3. Initial convergence of the closed-loop observers under no-fault scenarios.

4.1 Case 1: No fault scenario

Figure 4 depicts the behavior of the residual under a no-fault condition. Just after the convergence $(t=t_{conv})$, the residual is zero since both the closed-loop and open-loop observers have the same estimates. However, since there is no output feedback, the open-loop observers' performance degrades slightly after $t=t_{conv}$ due to the presence of uncertainty terms δ_p and δ_n while the closed-loop observers keep estimating the true states with reasonable accuracy. Accordingly, due to the differences between open- and closed-loop observers, the residuals reach a non-zero steady-state after some time. That non-zero steady-state is -100 mol/m^3 for the cathode residual r_p and -500 mol/m^3 for the anode residual r_n . Since the thresholds were to chosen based on non-faulty data, these steady-state values are well within threshold limits.

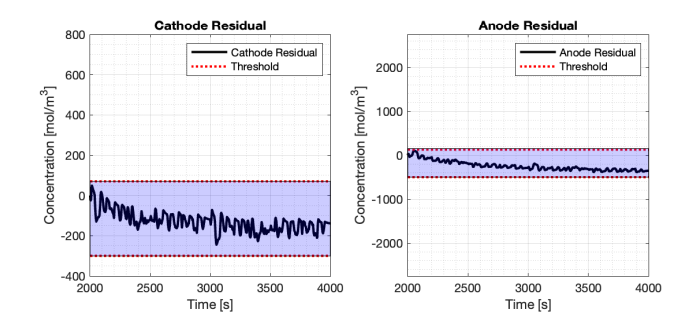


Fig. 4. Residual behavior under no fault scenario.

4.2 Case 2: Anode fault

Figure 5 depicts the behavior of the residuals in the presence of an anode fault. The anode fault is modeled at t = 2000 s by reducing the value of active surface area in negative electrode a_s^- by 30%. This reduces the nominal available volume of the solid part of anode due to the loss of active material, thereby reducing the process of intercalation. As shown in Table 1, the anode residual responded to the fault by eventually crossing the threshold while the cathode residual staved within the thresholds. This difference makes the anode's closed-loop observer to get closer to the actual value using the feedback. The anode residual finally settled around -800 mol/m^3 . Note that the cathode residual is also seen to have a slight surge of around -20 mol/m^3 . This is because of the fact that both the closed-loop observers require the voltage measurement in calculating the error for feedback. And since the fault is reflected in the voltage measurement, the cathode residual is also slightly influenced. However, the anode fault can easily isolated seeing a sharp surge in the anode residual value.

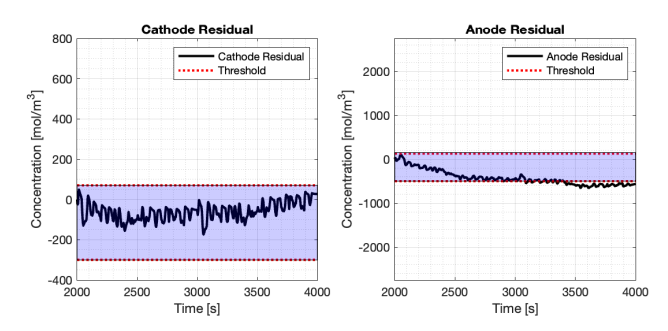


Fig. 5. Residual behavior under anode fault.

4.3 Case 3: Cathode Fault

Figure 6 depicts the behavior of the residuals in the presence of a cathode fault. The cathode fault is modeled at $t=2000~\rm s$ by reducing the value of active surface area in positive electrode a_s^+ by 50%. This reduces the nominal available volume of the solid part of cathode due to the loss of active material, thereby reducing the process of intercalation. As shown in Table 1, both the cathode and anode residuals are affected by the fault. This resulted in a ramp-like surge in the cathode residual to around $800~mol/m^3$. In addition to that, the anode residual is also seen to have a substantial steep change to around $-2000~mol/m^3$. This is because of two reasons. The closed-loop observer for both the electrodes require the voltage

measurement in calculating the error for feedback, which influences the anode residual slightly. However, the main contribution for this steep change is from the fact that the observers are designed in a cascaded manner. Since the state estimates from the cathode observer itself are not accurate, this further influences the anode observer to give wrong estimates as cathode observer estimates are given as inputs to the anode observer. So, whenever such a type of sharp surge is seen both anode and cathode residuals, it can be attributed to cathode fault.

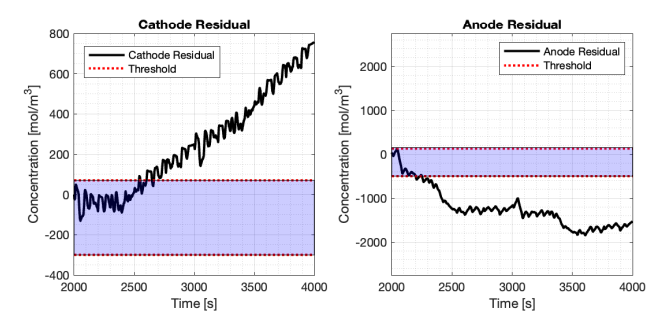


Fig. 6. Residual behavior under cathode fault.

5. CONCLUSIONS AND FUTURE WORK

This paper discusses the initial development of an observer based residual generator that can potentially be used to detect and isolate faults at the electrode level. The proposed approach is illustrated by a few simulation case studies. There are still a few challenges in the current approach that are yet to be addressed. One such challenge is the inability to isolate faults that affect both electrodes and faults that affect just the cathode. Fault estimation will also be addressed in the future work. A sensitivity study of the proposed approach with respect to the noise in the measurements and uncertainties in the model is also aimed to be performed in the future works.

6. ACKNOWLEDGMENTS

The authors would like to acknowledge the help provided by Mr. Shashank Dhananjay Vyas throughout this work.

REFERENCES

- Alavi, S.M., Samadi, M.F., and Saif, M. (2013). Plating mechanism detection in lithium-ion batteries, by using a particle-filtering based estimation technique. In 2013 American Control Conference, 4356–4361. IEEE.
- Allam, A. and Onori, S. (2018). An interconnected observer for concurrent estimation of bulk and surface concentration in the cathode and anode of a lithium-ion battery. *IEEE Transactions on Industrial Electronics*, 65(9), 7311–7321.
- Allam, A. and Onori, S. (2020). Online capacity estimation for lithium-ion battery cells via an electrochemical model-based adaptive interconnected observer. *IEEE Transactions on Control Systems Technology*, 29(4), 1636–1651.
- Dey, S. and Ayalew, B. (2015). A diagnostic scheme for detection, isolation and estimation of electrochemical faults in lithium-ion cells. In *Dynamic Systems and Control Conference*, volume 57243, V001T13A001. American Society of Mechanical Engineers.

- Dey, S. and Ayalew, B. (2017). Real-time estimation of lithium-ion concentration in both electrodes of a lithium-ion battery cell utilizing electrochemical—thermal coupling. *Journal of Dynamic Systems, Measurement, and Control*, 139(3).
- Dey, S., Perez, H.E., and Moura, S.J. (2017). Model-based battery thermal fault diagnostics: Algorithms, analysis, and experiments. *IEEE Transactions on Control Systems Technology*, 27(2), 576–587.
- Dey, S., Shi, Y., Smith, K., Colclasure, A.M., and Li, X. (2020). From battery cell to electrodes: Real-time estimation of charge and health of individual battery electrodes. *IEEE Transactions on Industrial Electronics*, 67(3), 2167–2175. doi:10.1109/TIE.2019.2907514.
- Lee, S. and Kim, Y. (2020). Li-ion battery electrode health diagnostics using machine learning. In 2020 American Control Conference (ACC), 1137–1142. IEEE.
- Li, W., Zhang, J., Ringbeck, F., Jöst, D., Zhang, L., Wei, Z., and Sauer, D.U. (2021). Physics-informed neural networks for electrode-level state estimation in lithiumion batteries. *Journal of Power Sources*, 506, 230034.
- Liu, Z., Ahmed, Q., Rizzoni, G., and He, H. (2014). Fault detection and isolation for lithium-ion battery system using structural analysis and sequential residual generation. In *Dynamic Systems and Control Conference*, volume 46193, V002T36A005. American Society of Mechanical Engineers.
- Marcicki, J., Canova, M., Conlisk, A.T., and Rizzoni, G. (2013). Design and parametrization analysis of a reduced-order electrochemical model of graphite/lifepo4 cells for soc/soh estimation. *Journal of Power Sources*, 237, 310–324.
- Mohtat, P., Lee, S., Siegel, J.B., and Stefanopoulou, A.G. (2019). Towards better estimability of electrode-specific state of health: Decoding the cell expansion. *Journal of Power Sources*, 427, 101–111.
- Moura, S.J., Argomedo, F.B., Klein, R., Mirtabatabaei, A., and Krstic, M. (2016). Battery state estimation for a single particle model with electrolyte dynamics. *IEEE Transactions on Control Systems Technology*, 25(2), 453–468.
- Rahimian, S.K., Rayman, S., and White, R.E. (2012). State of charge and loss of active material estimation of a lithium ion cell under low earth orbit condition using kalman filtering approaches. *Journal of the Electrochemical Society*, 159(6), A860.
- Rahn, C.D. and Wang, C.Y. (2013). Battery systems engineering. John Wiley & Sons.
- Sattarzadeh, S., Dey, S., Colclasure, A., and Smith, K. (2020). Addressing the observability problem in batteries: Algorithm design for electrodelevel charge and health estimation. In 2020 American Control Conference (ACC), 1131–1136. doi: 10.23919/ACC45564.2020.9147307.
- Zhang, D., Couto, L.D., and Moura, S.J. (2021). Electrode-level state estimation in lithium-ion batteries via kalman decomposition. *IEEE Control Systems Letters*, 5(5), 1657–1662. doi: 10.1109/LCSYS.2020.3042751.